Supplementary Material

We provide additional data and specifications that we use to support the statements in the main text. The Supplementary Material is organized as follows:

- **A: System characterization**
- **B: VMC control, theoretical formulation for the apparatus**
- **C: Full force and stiffness theorem, CCT correction, and optimization for online tuning**
- **D: Description of additional experiments**
- **E: Description of videos**
- **F: Description of further results**

A: System characterization

This section reports the experimental characterization of the two platforms:

1. **Finger kinematics**
2. **Hand kinematics**
3. **Friction compensation validation**
4. **Identified parameters**

A.1: Finger kinematics

The virtual model controller maps forces onto the actuators through the transmission Jacobian $\mathbf{J}_{\boldsymbol{\theta}} = \partial\boldsymbol{\theta}/\partial\mathbf{q}$, where $\mathbf{q}$ collects the actuator angles and $\boldsymbol{\theta}$ the joint angles. This mapping presupposes that the actuator-to-joint relation is linear, that is:

$$\theta_{\mathrm{MCP}} = \frac{r_p}{r_m}\, q_{\mathrm{MCP}}, \qquad \theta_{\mathrm{PIP}} = \frac{r_m}{c}\, q_{\mathrm{PIP}}, \qquad \theta_{\mathrm{DIP}} = \theta_{\mathrm{PIP}}, \tag{S1}$$

with r_m the actuator pulley radius, r_p the finger MCP pulley radius, and c a cable-driven transmission constant. We verified this assumption directly on every joint of both platforms.

Joint angles were measured with a goniometer while each actuator was driven through its admissible range, and a linear model was fitted to the resulting pairs. Fig. S1 reports the single-finger test bed in terms of both actuation routing and joint calibration. The DIP joint is not calibrated independently, being mechanically constrained to follow the PIP.

A.2: Hand kinematics

The same procedure was applied to every digit of the ADAPT Hand. Fig. S2 reports the thumb, whose four joints (CMC1, CMC2, MCP, IP) are driven by a dedicated actuator, and Fig. S3 the MCP and PIP joints of the index, middle, ring, and pinky. As on the test bed, the DIP follows

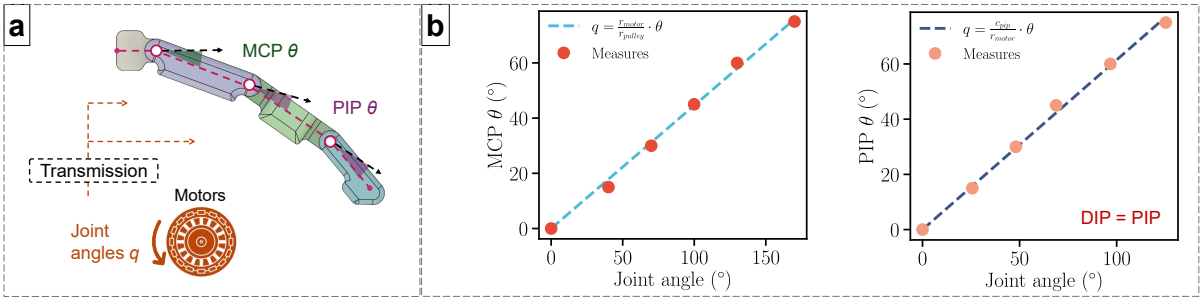

Figure S1: **Kinematic transmission calibration of the finger test bed**. **a** Schematic of the motor-to-joint transmission, relating motor rotation to the MCP and PIP joint angles. **b** Calibration of the MCP (left) and PIP (right) joint angles against motor angles, with linear fits to the measured points; the DIP joint is mechanically coupled to PIP.

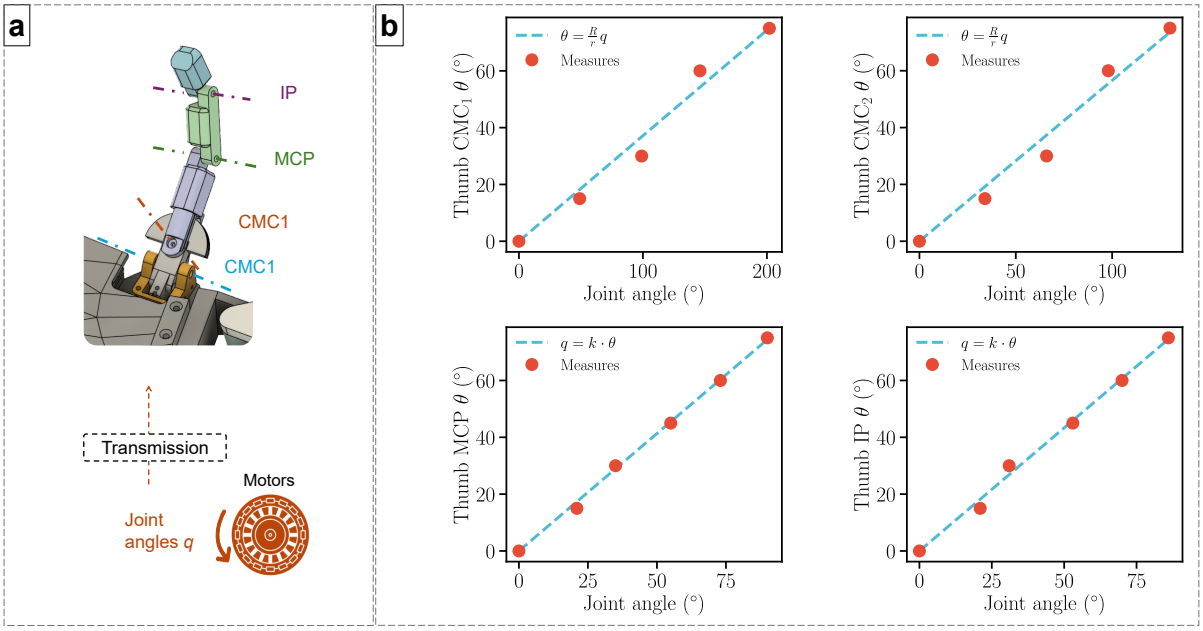

Figure S2: **Kinematic transmission calibration of the thumb**. **a** Thumb kinematic diagram, with the CMC1, CMC2, MCP, and IP joints and their motor transmission. **b** Calibration of the CMC1, CMC2, MCP, and IP joint angles against motor angle, with linear fits to the measured points.

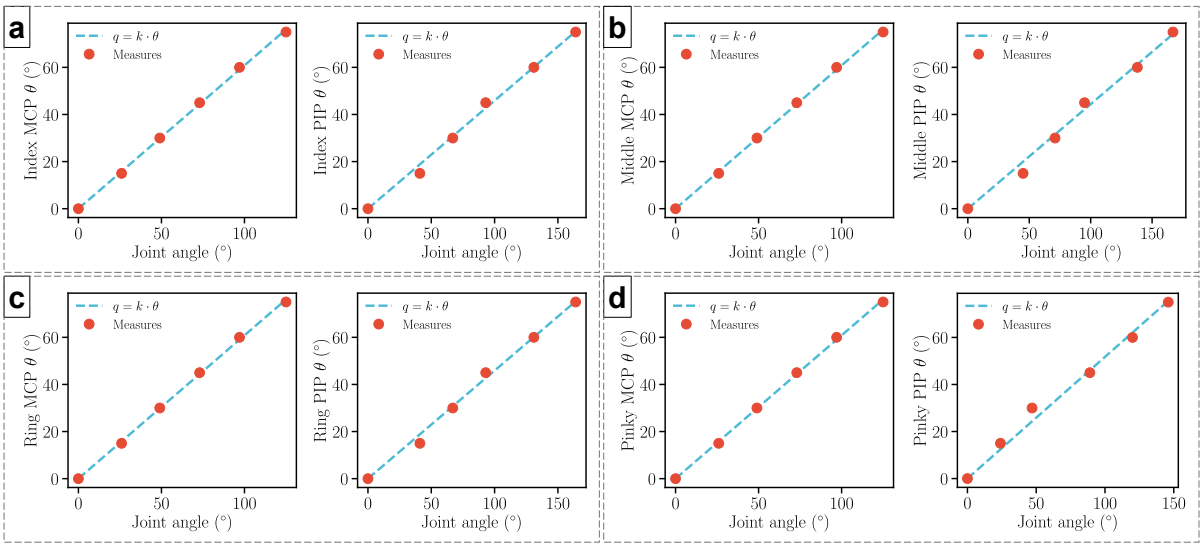

Figure S3: **Kinematic transmission calibration of the index, middle, ring, and pinky fingers**. **a** Index MCP and PIP calibration. **b** Middle MCP and PIP calibration. **c** Ring MCP and PIP calibration. **d** Pinky MCP and PIP calibration.

the PIP through a mimic coupling and is not calibrated separately. The fitted slopes give the transmission constants of Table S3. Differences between the constants of the hand and of the finger reflect their different transmission designs.

A.3: Finger friction compensation validation

Actuator stiction is compensated by a Stribeck term whose envelope is largest at low velocity:

$$\boldsymbol{\tau}_f = F_{\max}\, \exp\!\left(-\left(\dot{\mathbf{q}}/v_{\lim}\right)^2\right) \odot \operatorname{sign}(\boldsymbol{\tau}_{\mathrm{cmd}})\,, \tag{S2}$$

with $\odot$ the element-wise product. Since the envelope decays with velocity, the compensation pushes the actuator into motion and switches itself off, producing a continuous low-amplitude oscillation. To validate it (Fig. S4**a**), the finger was controlled in free space with torsional virtual springs, tracking a step and a ramp reference with and without the Stribeck term. Without compensation both joints exhibit a dead band: small commanded torques produce no motion until the stiction is exceeded, leaving a steady-state offset between the commanded and the

Table S1: **Notation: kinematics and virtual elements**. Bold lowercase denotes vectors, bold uppercase matrices.

Symbol	Meaning	Unit
Coordinates and kinematics		
$\mathbf{q}$	Actuator (motor) angles	rad
$\boldsymbol{\theta}$	Joint angles (MCP, PIP, DIP)	rad
$\mathbf{x}$	Position of the output point, typically the fingertip	m
$\mathbf{d}$	Generalized coordinate hosting a virtual element	varies
$\mathbf{J}_{\boldsymbol{\theta}}$	Transmission Jacobian, $\partial\boldsymbol{\theta}/\partial\mathbf{q}$	—
$\mathbf{J}_x$	Output Jacobian, $\partial\mathbf{x}/\partial\mathbf{q}$	m/rad
$\mathbf{J}_d$	Virtual-element Jacobian, $\partial\mathbf{d}/\partial\mathbf{q}$	varies
ℓ_p, ℓ_m, ℓ_d	Proximal, middle, distal phalanx lengths	m
$r_m,\ r_p$	Actuator and finger MCP pulley radii	m
c	Cable-driven transmission constant	m
Virtual elements		
$\mathbf{K}_d,\ \mathbf{D}_d$	Virtual stiffness and damping on $\mathbf{d}$	varies
$\mathbf{d}_{\text{ref}}, \mathbf{e}$	Virtual rest configuration; deflection $\mathbf{d}_{\text{ref}} - \mathbf{d}$	varies
$\boldsymbol{\tau}_d$	Generalized virtual force, $\mathbf{K}_d\mathbf{e}$	varies
U	Storage function (potential) of an element	J
K_θ	Shared scalar torsional stiffness, finger-space configuration	N·m/rad
K_c	Cart-constrained fingertip stiffness, test bed	N/m
K_t	Fingertip cartesian stiffness, hand	N/m
K_{sensing}	Thumb stiffness during compliance probing	N/m
$A,\ \sigma,\ \Delta\mathbf{z}$	Gaussian strength, width, offset from the repulsion center	N/m, m, m
α	Rate of a stiffness law; *also* the gradient-descent step size	varies
p	Order of the polynomial stiffness law	—
ϕ	Cart direction angle in the sagittal plane	deg

Table S2: **Notation: contact, adaptation, and analysis**. Bold lowercase denotes vectors, bold uppercase matrices.

Symbol	Meaning	Unit
Contact, force, and stiffness		
$\mathbf{n}$	Contact normal (unit); *distinct* from the sample count N	—
$\mathbf{P} = \mathbf{n}\mathbf{n}^T$	Contact projection, acting on the *output*	—
$\mathbf{P}_c = \mathbf{n}_c\mathbf{n}_c^T$	Cart projection, acting on the *virtual element*	—
$\boldsymbol{\eta}$	Diagonal transmission efficiency, $\eta_i \in (0, 1]$	—
$\mathbf{f}_x$, $F = \mathbf{n}^T\mathbf{f}_x$	Contact force at the output; its normal component	N
$\mathbf{K}_x$, $K_n = \mathbf{n}^T\mathbf{K}_x\mathbf{n}$	Output stiffness; its normal component	N/m
$(\cdot)^*$	Moore–Penrose pseudoinverse	—
Adaptation, stability, and analysis		
$\mathcal{L}$	Force-tracking loss, $\frac{1}{2}\|\mathbf{f}_x - \mathbf{f}_{x,\mathrm{ref}}\|^2$	N^2
$\mathbf{L}$, $\mathbf{R}$	Congruence maps in $\mathbf{K}_x = \mathbf{L}\mathbf{K}_d\mathbf{R}$	varies
$\mathbf{S}$	Sensitivity of the force to the rest configuration	varies
e_i, $\mathbf{e}_i$	Scalar and vector force error at iteration i	N
γ_i, λ_i, β_i	Step-size bounds in Lemma 1 and Proposition 3	varies
ς	$\|\mathbf{K}_{\mathrm{skew}}\|_2$, asymmetry of $\mathbf{K}_d$	varies
d	Imposed arm displacement; *distinct* from the vector $\mathbf{d}$	m
$\Delta F/\Delta d$	Effective stiffness, by regression over the descent window	N/m
$\tilde{F}$	Smoothed normal force (Savitzky–Golay, window 21, order 3)	N
N	Number of independent repetitions per condition	—

Table S3: **Identified and measured parameters**. Values used by the controller and by the stiffness model on both platforms.

Parameter	Value	Unit
Link geometry (both platforms)		
Phalanx lengths $\ell_p,\ \ell_m,\ \ell_d$	40.0, 30.0, 17.5	mm
Fingertip offset along the distal axis	17.5	mm
Transmission, single-finger test bed		
Actuator pulley r_m	5.00	mm
Finger MCP pulley r_p	2.23	mm
PIP transmission constant c	8.13	mm
Transmission, ADAPT Hand		
Actuator pulley r_m, all digits	5.00	mm
Finger MCP pulley r_p, four fingers	3.04	mm
c: index / middle / ring / pinky	10.90 / 11.27 / 10.90 / 9.67	mm
Thumb CMC1 / CMC2 pulley radii	13.46 / 8.83	mm
Thumb MCP / IP transmission constants	6.05 / 5.77	mm
Wrist spur / bevel reduction	0.800 / 0.857	—
Spread ratios: index / middle / ring / pinky	1.0 / 0 / -1.0 / -1.5	—
Transmission efficiency (identified)		
η_{MCP}, all MCP-type axes	0.837	—
η_{PIP}, all PIP-type axes	0.359	—
η, thumb CMC1, CMC2, and spread	1.0 (assumed)	—
Friction compensation		
Stribeck velocity v_{lim}, both platforms	0.03	rad/s
$F_{\max}$, single-finger test bed	0.20	N·m
$F_{\max}$, hand: guitar / weight bearing	0.02 / 0.01	N·m
$F_{\max}$, hand: in-hand and dynamic grasp	0.06	N·m
$F_{\max}$, hand: compliance sensing / apple	0.04 / 0.05	N·m
Limits and control		
Deadzone limit stiffness, finger / hand	1.0 / 0.6	N·m/rad
Commanded torque saturation	0.8	N·m
Joint range, MCP	$[0,\ \pi/2]$	rad
Joint range, PIP and DIP	$[0,\ 1.22]$	rad
Control rate, finger / hand	900 / 330	Hz
Torque-controlled actuators, finger / hand	2 / 13	—

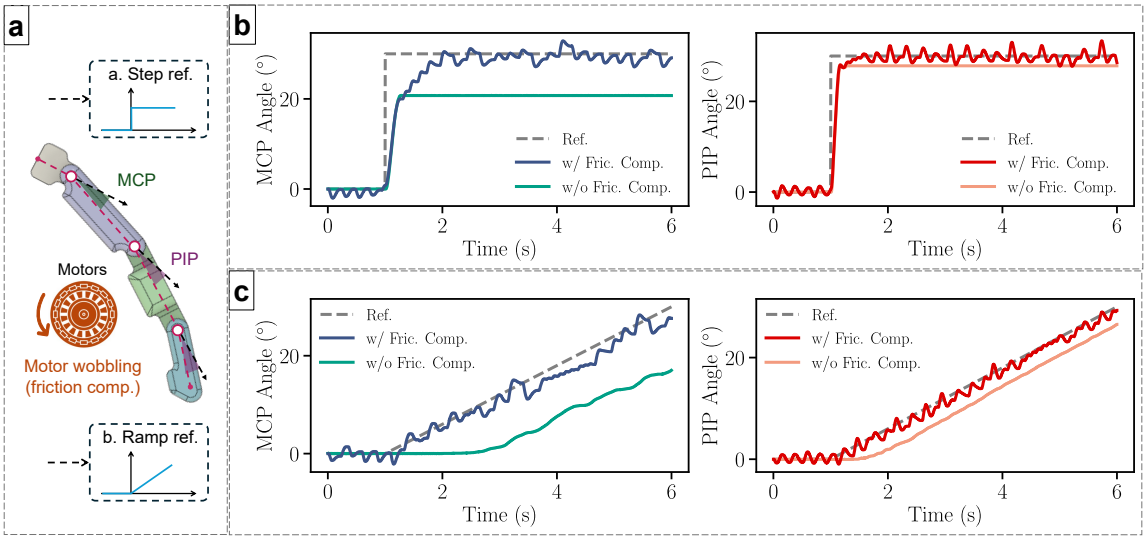

Figure S4: **Validation of friction compensation via continuous motor wobbling**. **a** Friction-compensation scheme: continuous motor wobbling superimposed on the reference command, tested against a step and a ramp reference. **b** Step response of the MCP and PIP joints, with and without friction compensation. **c** Ramp response of the MCP and PIP joints, with and without friction compensation.

reached joint angle (Fig. S4**b**), and under a ramp reference the same effect appears as stick–slip (Fig. S4**c**). With compensation the dead band is removed and tracking becomes continuous at both joints, the MCP benefiting more, at the cost of a persistent ripple at the joint and, consequently, in the measured contact force. The trade is favorable here because the forces of interest are small: a dead band of the order of the stiction torque would suppress precisely the low-force regime in which the compliance modulation operates. The ripple can be removed at analysis time by the smoothing described in the Methods.

A.4: Identified parameters

Table S1 and Table S2 list the notation used throughout the main text and this document. Table S3 collects every identified and measured parameter. All values are those used by the controller and by the stiffness model, and corresponds to the constants defined in the code repository.

B: VMC control, theoretical formulation for the apparatus

This section gives the complete element library, with the force and the stored energy of each element, and then the concrete virtual-element configurations used on the two platforms.

B.1: Element library and storage functions

Let $\mathbf{e} = \mathbf{d}_{\mathrm{ref}} - \mathbf{d}$ denote the deflection of an element and $\dot{\mathbf{d}}$ its rate. Each spring is specified by the force it returns: the actuator torque follows by mapping that force through $\mathbf{J}_d^T$ and summing over elements. Every spring below is conservative, and we give its storage function U explicitly, since $\mathbf{F} = -\partial U/\partial \mathbf{d}$ with $U \geq 0$ and $U(\mathbf{0}) = 0$ is what makes the element passive. Dampers store nothing and are characterized instead by the power they dissipate.

Linear spring and damper. The baseline elements, used wherever no other law is stated:

$$\mathbf{F} = \mathbf{K}_d\,\mathbf{e}, \qquad U = \tfrac{1}{2}\,\mathbf{e}^T\mathbf{K}_d\,\mathbf{e}, \qquad \mathbf{F} = -\mathbf{D}_d\,\dot{\mathbf{d}}, \qquad \mathcal{P} = \dot{\mathbf{d}}^T\mathbf{D}_d\,\dot{\mathbf{d}} \geq 0. \tag{S3}$$

$U \geq 0$ for $\mathbf{K}_d \succeq 0$ and $\mathcal{P} \geq 0$ for $\mathbf{D}_d \succeq 0$, so the pair is passive for any admissible gains.

Cart-constrained elements. A cart admits motion along a single direction $\mathbf{n}_c$ and resists nothing in the orthogonal complement. With $\mathbf{P}_c = \mathbf{n}_c\mathbf{n}_c^T$ the gain is projected on both sides, which keeps the element symmetric and stores no energy in the constrained directions:

$$\mathbf{F} = \mathbf{P}_c\,\mathbf{K}_d\,\mathbf{P}_c\,\mathbf{e}, \qquad U = \tfrac{1}{2}\,\mathbf{e}^T\mathbf{P}_c\,\mathbf{K}_d\,\mathbf{P}_c\,\mathbf{e}, \qquad \mathbf{F} = -\mathbf{P}_c\,\mathbf{D}_d\,\mathbf{P}_c\,\dot{\mathbf{d}}. \tag{S4}$$

Since $\mathbf{P}_c\mathbf{K}_d\mathbf{P}_c \succeq 0$ whenever $\mathbf{K}_d \succeq 0$, the cart element is passive. Rotating $\mathbf{n}_c$ in the sagittal plane by an angle ϕ produces the directional responses reported in the main text.

Gaussian repulsive spring. A bounded repulsive field that decays with distance, used to reshape the force response over part of the stroke while leaving it unchanged elsewhere. With $\Delta\mathbf{z}$

the offset from the repulsion center,

$$\mathbf{F}_g = A \exp\left(-\frac{\|\Delta\mathbf{z}\|^2}{2\sigma^2}\right) \Delta\mathbf{z}, \qquad U_g = A\,\sigma^2 \exp\left(-\frac{\|\Delta\mathbf{z}\|^2}{2\sigma^2}\right). \tag{S5}$$

Direct differentiation confirms $\mathbf{F}_g = -\partial U_g / \partial \Delta\mathbf{z}$. The potential is a bounded barrier of height $A\sigma^2$ at the center, decaying to zero far from it, so the element can store only a finite amount of energy. The force magnitude vanishes both at the center and at infinity and peaks at $\|\Delta\mathbf{z}\| = \sigma$. A cart-constrained variant replaces $\Delta\mathbf{z}$ by $\mathbf{P}_c\Delta\mathbf{z}$ and projects the result.

Deadzone limit spring. Joint limits are enforced by an element inactive inside $[\theta_-, \theta_+]$ and linear outside it:

$$\begin{aligned} \tau_{\text{lim}} &= K_{\text{lim}} \left[\max(\theta_- - \theta, 0) - \max(\theta - \theta_+, 0)\right], \\ U_{\text{lim}} &= \tfrac{1}{2} K_{\text{lim}} \left[\max(\theta_- - \theta, 0)^2 + \max(\theta - \theta_+, 0)^2\right]. \end{aligned} \tag{S6}$$

U_{lim} is continuous and continuously differentiable at both breakpoints, so the element is conservative and does not compromise passivity.

B.2: Stiffness laws and the limits of the potential argument

Two families of element schedule their stiffness during the interaction rather than holding it fixed. Whether a potential still exists depends on *what the stiffness is scheduled on*, and the distinction separates the experiments that remain passive from those that do not.

Scheduled on the element's own deflection. If the stiffness depends only on the deflection of the element itself, the force $F(e) = K(e)\,e$ is a memoryless function of e and a potential always exists:

$$U(e) = \int_0^e K(\xi)\,\xi\,\mathrm{d}\xi \;\geq\; 0 \quad \text{for } K(\cdot) \geq 0, \tag{S7}$$

so the element is passive however sharply the stiffness varies. For the polynomial law the integral is elementary,

$$K(d) = K_0 \left(\frac{d}{d_{\text{norm}}} \right)^p, \qquad U(d) = \frac{K_0 \, d^{p+2}}{(p+2) \, d_{\text{norm}}^p}, \tag{S8}$$

recovering the linear spring at $p = 0$. For the sigmoidal law,

$$K(d) = K_{\max} - \frac{K_{\max} - K_{\min}}{1 + e^{-\alpha(d - d_{\text{th}})}}, \tag{S9}$$

which switches between two regimes about a threshold d_{th} at a rate set by α, the integral of Eq. (S7) has no elementary closed form but is bounded between the potentials of the two linear springs $K_{\min}$ and $K_{\max}$, and is evaluated numerically. The polynomial stiffness is also clamped below at $K_{\min}$ near $d = 0$ for numerical stability.

Scheduled on an exogenous signal. The contact-dependent laws are different. Here the stiffness is a function of the measured contact force F:

$$K_\theta^{\uparrow}(F) = K_{\min} + (K_{\max} - K_{\min}) \left(1 - e^{-\alpha F} \right) \tag{S10}$$

$$K_\theta^{\downarrow}(F) = K_{\min} + (K_{\max} - K_{\min}) \, e^{-\alpha F} \tag{S11}$$

for stiffening and softening respectively. Both reach the midpoint of $[K_{\min}, K_{\max}]$ at the half-transition force $F_{1/2} = \ln 2 / \alpha$, which is how the swept values of α were chosen to span the accessible force range logarithmically; $\alpha = 0$ recovers a constant stiffness, $K_{\min}$ for stiffening and $K_{\max}$ for softening, giving the baseline against which each is compared.

Because F is an external measurement rather than a function of the element's own state, the torque is no longer a memoryless function of the deflection and no potential exists: these elements are not passive by construction, and the same holds for any law scheduled on the arm displacement rather than on the element's deflection. The energy they can inject is nonetheless bounded, since the stiffness is confined to $[K_{\min}, K_{\max}]$ and the stored energy at any deflection therefore lies between the potentials of the two extreme linear springs.

B.3: Configurations on the single-finger test bed

The actuator vector is $\mathbf{q} = [q_{\mathrm{MCP}}, q_{\mathrm{PIP}}]^T$ and the joint vector $\boldsymbol{\theta} = [\theta_{\mathrm{MCP}}, \theta_{\mathrm{PIP}}, \theta_{\mathrm{DIP}}]^T$, related by Eq. (S1). Three main configurations are defined and used.

In the *finger-space* configuration the virtual coordinate is the joint vector itself, $\mathbf{d} = \boldsymbol{\theta}$, so $\mathbf{J}_d = \mathbf{J}_{\boldsymbol{\theta}} \in \mathbb{R}^{3\times 2}$, constant and given by the transmission ratios. With a shared stiffness, $\mathbf{K}_d = K_\theta \mathbf{I}_3$. Note that $\mathbf{J}_d$ has more rows than columns: three virtual coordinates are driven by two actuators, so the elements are not independently realizable and only their projection onto the actuator space is transmitted. In the *task-space* configuration the virtual coordinate is the position of a point on the distal phalanx, $\mathbf{d} = \mathbf{x}_{\mathrm{tip}} \in \mathbb{R}^3$, and $\mathbf{J}_d = \mathbf{J}_x \in \mathbb{R}^{3\times 2}$ is configuration-dependent. A cart constraint is imposed as in Eq. (S4). The cart projection $\mathbf{P}_c$ acts on the virtual element and must not be confused with the contact projection $\mathbf{P} = \mathbf{n}\mathbf{n}^T$, which acts on the output. The *mixed-space* configuration concatenates the two, $\mathbf{d} = [\boldsymbol{\theta}^T, \mathbf{x}_{\mathrm{tip}}^T]^T \in \mathbb{R}^6$, with $\mathbf{J}_d$ the vertical stacking of $\mathbf{J}_{\boldsymbol{\theta}}$ and $\mathbf{J}_x$, and $\mathbf{K}_d$ block-diagonal.

B.4: Configurations on the ADAPT Hand

The thirteen torque-controlled actuators are ordered as thumb CMC1, CMC2, MCP, and IP; the spread actuator; and then MCP and PIP for index, middle, ring, and pinky. The wrist actuators are held in position mode and do not appear in $\mathbf{q}$. Each digit contributes an independent block. Joint-space elements act on the flexion chain of each digit, giving a block-diagonal $\mathbf{K}_d$ with one block per digit; the spread joints of all four fingers are driven by a single actuator through fixed motion ratios, so their four virtual elements share one column of $\mathbf{J}_d$ and cannot be set independently. Task-space elements are attached to the five fingertips. Since the digits are kinematically independent, $\mathbf{J}_d$ is block-diagonal for these elements too. Task-space rest position are often placed by evaluating the forward kinematics at joint targets taken along the first principal component of human grasp postures. The specific joint targets differ between tasks.

C: Full force and stiffness theorem, CCT correction, and optimization for online tuning

C.1: General derivation

Let $\mathbf{q}$ be the actuator vector, $\mathbf{x}$ the output point, and $\mathbf{d}$ a vector of generalized coordinates hosting the virtual elements, with Jacobians $\mathbf{J}_x = \partial\mathbf{x}/\partial\mathbf{q}$ and $\mathbf{J}_d = \partial\mathbf{d}/\partial\mathbf{q}$. Let $\mathbf{P}$ project onto the directions along which the output performs virtual work (i.e., a force $\mathbf{f}_x$ is applied), and let $\boldsymbol{\eta}$ be the diagonal transmission efficiency in actuator space. The generalized virtual force in static conditions, without damping contributions, is $\boldsymbol{\tau}_d = \mathbf{K}_d(\mathbf{d}_{\text{ref}} - \mathbf{d})$.

Equating the virtual work performed by the elements to that performed at the output, and substituting $\dot{\mathbf{d}} = \mathbf{J}_d\dot{\mathbf{q}}$ and $\dot{\mathbf{x}} = \mathbf{J}_x\dot{\mathbf{q}}$, gives for arbitrary $\dot{\mathbf{q}}$ the balance:

$$\boldsymbol{\eta}\,\mathbf{J}_d^T\boldsymbol{\tau}_d = (\mathbf{P}\mathbf{J}_x)^T\,\mathbf{f}_x, \tag{S12}$$

whose least-squares solution is the contact force:

$$\mathbf{f}_x = ((\mathbf{P}\mathbf{J}_x)^*)^T\,\boldsymbol{\eta}\,\mathbf{J}_d^T\,\mathbf{K}_d\,(\mathbf{d}_{\text{ref}} - \mathbf{d})\,. \tag{S13}$$

Theorem 1 (VMC stiffness composition)**.** *Consider a tendon-driven system with actuator vector* $\mathbf{q} \in \mathbb{R}^{n_q}$*, output Jacobian* $\mathbf{J}_x$*, output projection* $\mathbf{P}$*, and diagonal transmission efficiency* $\boldsymbol{\eta}$ *with entries in* $(0, 1]$*, constant with respect to* $\mathbf{q}$*. Let a set of virtual elements be defined on generalized coordinates* $\mathbf{d}$ *with Jacobian* $\mathbf{J}_d$ *and positive semi-definite stiffness* $\mathbf{K}_d$*. Then the output-space stiffness is, to first order,*

$$\mathbf{K}_x = ((\mathbf{P}\mathbf{J}_x)^*)^T\,\boldsymbol{\eta}\,\mathbf{J}_d^T\mathbf{K}_d\mathbf{J}_d\,(\mathbf{P}\mathbf{J}_x)^*,$$

and, if the elements are decoupled so that $\mathbf{K}_d$ *is block-diagonal with blocks* k_i*,*

$$\mathbf{K}_x = ((\mathbf{P}\mathbf{J}_x)^*)^T\,\boldsymbol{\eta}\left(\sum_i \mathbf{J}_{d_i}^T\,k_i\,\mathbf{J}_{d_i}\right)(\mathbf{P}\mathbf{J}_x)^*.$$

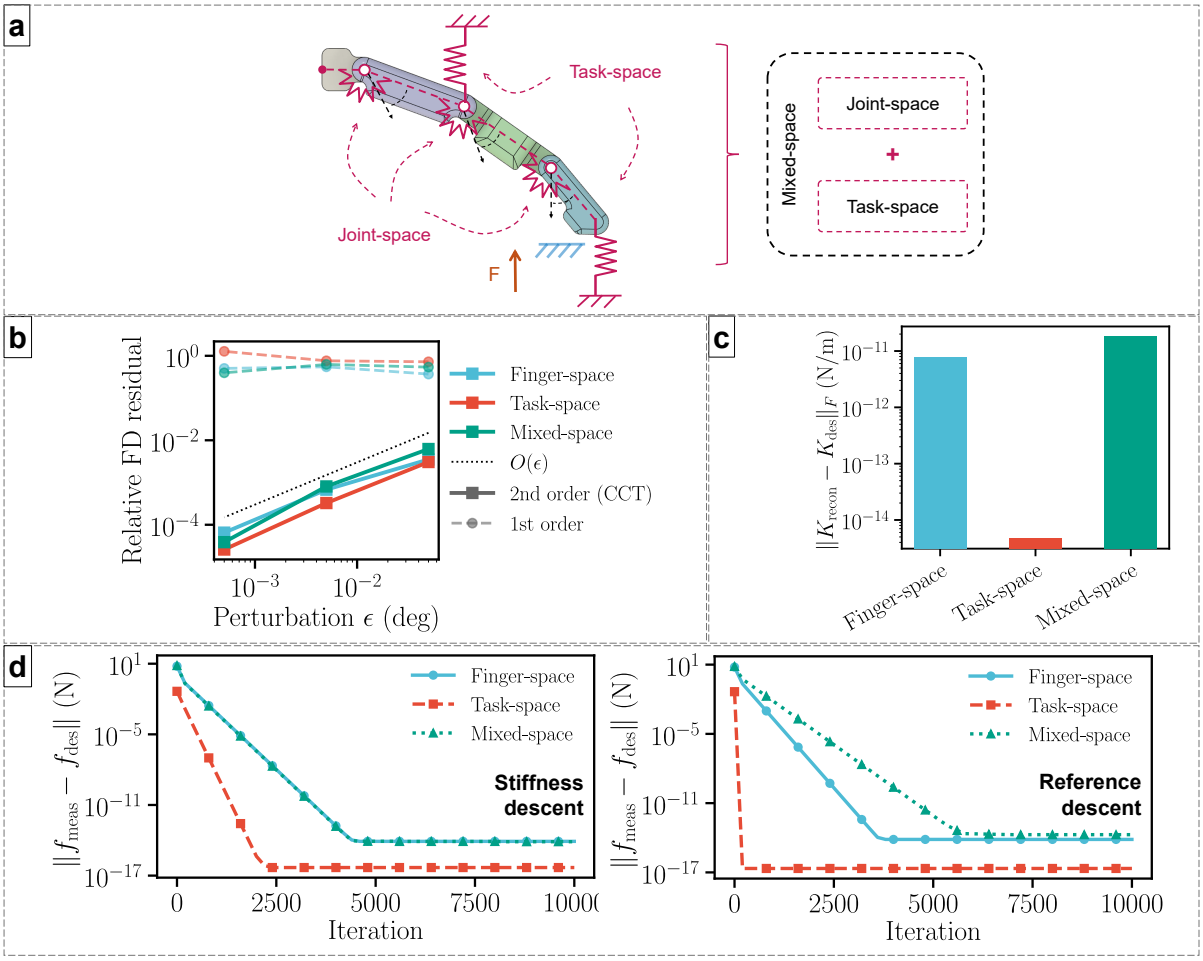

Figure S5: **Numerical validation of the VMC stiffness model and of the force-tracking gradient descent on the single-finger platform**. **a** Finger-space, task-space, and mixed-space virtual element configuration used for validation. **b** Relative residual between the analytically predicted stiffness and a local, finite-difference estimated obtained by perturbing the configuration, as a function of perturbation size, compared to first-order and second-order (CCT-corrected) predictions. **c** Fröbenius-norm error of the feed-forward stiffness inversion: the task-space stiffness achieved by inverting a desired stiffness into virtual-element parameters, compared to that desired stiffness, fo reach configuration. **d** Convergence of the force error during gradient-descent adaptation of the virtual stiffness (left) and the virtual reference (right), across the three control configurations.

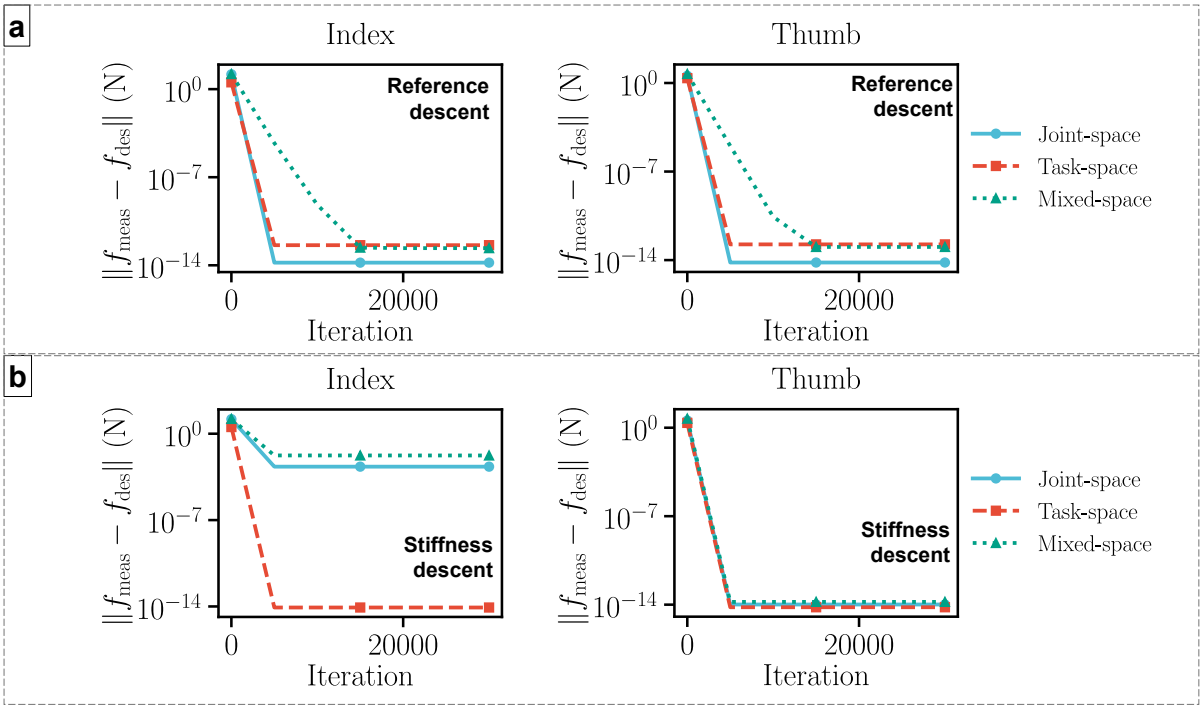

Figure S6: **Convergence of force-tracking gradient descent on the hand platform**. **a** Convergence of the force error during reference-descent adaptation for the index and thumb fingers, across joint-space, task-space, and mixed-space virtual elements. **b** Convergence of the force error during stiffness-descent adaptation for the index and thumb fingers, across the same three configurations.

The force and stiffness at the output are therefore fully determined by the virtual parameters, the kinematic structure, the transmission efficiency, and the output projection, and contributions from elements defined in different coordinate spaces compose additively.

Proof. Differentiate Eq. (S12) with respect to $\mathbf{q}$. Writing $d\boldsymbol{\tau}_d = -\mathbf{K}_d\, d\mathbf{d} = -\mathbf{K}_d\mathbf{J}_d\, d\mathbf{q}$ and $d\mathbf{f}_x = -\mathbf{K}_x\, d(\mathbf{P}\mathbf{x}) = -\mathbf{K}_x\mathbf{P}\mathbf{J}_x\, d\mathbf{q}$, and retaining only the terms in which the Jacobians are held constant, gives

$$-\boldsymbol{\eta}\,\mathbf{J}_d^T\mathbf{K}_d\mathbf{J}_d = -\left(\mathbf{P}\mathbf{J}_x\right)^T\mathbf{K}_x\left(\mathbf{P}\mathbf{J}_x\right).$$

Solving in the least-squares sense yields the stated expression. The decoupled form follows by partitioning $\mathbf{J}_d$ row-wise into the blocks associated with each element and expanding the block-diagonal $\mathbf{K}_d$, the cross terms vanishing. Since the derivation nowhere inverts $\mathbf{J}_d$, no rank condition on $\mathbf{J}_d$ is needed. □

Corollary 2 (Exact second-order stiffness)**.** *Retaining the terms in which the Jacobians vary with configuration,*

$$\mathbf{K}_x = \left((\mathbf{P}\mathbf{J}_x)^*\right)^T\left[\boldsymbol{\eta}\,\mathbf{J}_d^T\mathbf{K}_d\mathbf{J}_d + \frac{\partial(\mathbf{P}\mathbf{J}_x)^T}{\partial\mathbf{q}}\,\mathbf{f}_x - \frac{\partial(\boldsymbol{\eta}\,\mathbf{J}_d^T)}{\partial\mathbf{q}}\,\boldsymbol{\tau}_d\right](\mathbf{P}\mathbf{J}_x)^*. \tag{S14}$$

The two correction terms are the geometric stiffness contributions, involving the Hessians of the output and virtual-element Jacobians weighted respectively by the external force and by the virtual torque.

Proof. Immediate from the same differentiation, retaining the Jacobian derivatives. Both Hessians are available analytically from the symbolic kinematic model, so Eq. (S14) is evaluable at every control cycle. □

C.2: Feed-forward inversion with several element groups

Consider first a single group of virtual elements. Theorem 1 gives $\mathbf{K}_x = \mathbf{L}\mathbf{K}_d\mathbf{R}$ with $\mathbf{L} = \left((\mathbf{P}\mathbf{J}_x)^*\right)^T\boldsymbol{\eta}\,\mathbf{J}_d^T$ and $\mathbf{R} = \mathbf{J}_d(\mathbf{P}\mathbf{J}_x)^*$, both fixed at the current configuration. The unknown $\mathbf{K}_d$

appears between the two maps, so the relation is not in the form of a single matrix acting on a vector of unknowns and cannot be inverted directly. Applying the identity $\mathrm{vec}(\mathbf{AXB}) = (\mathbf{B}^T \otimes \mathbf{A})\,\mathrm{vec}(\mathbf{X})$ with $\mathbf{A} = \mathbf{L}$, $\mathbf{X} = \mathbf{K}_d$ and $\mathbf{B} = \mathbf{R}$:

$$\mathrm{vec}(\mathbf{K}_x) = \left(\mathbf{R}^T \otimes \mathbf{L}\right)\mathrm{vec}(\mathbf{K}_d) =: \mathbf{M}\,\mathrm{vec}(\mathbf{K}_d), \tag{S15}$$

a linear system in the stacked unknowns. Inverting it in the least-squares sense:

$$\mathrm{vec}\left(\mathbf{K}_d^{\mathrm{ff}}\right) = \mathbf{M}^*\,\mathrm{vec}(\mathbf{K}_{x,\mathrm{des}})\,. \tag{S16}$$

Because $\|\,\mathrm{vec}(\mathbf{X})\|_2 = \|\mathbf{X}\|_F$, the residual minimized by the pseudoinverse is the Frobenius distance $\|\mathbf{L}\mathbf{K}_d\mathbf{R} - \mathbf{K}_{x,\mathrm{des}}\|_F$, and among all minimizers the solution returned is the one of smallest $\|\mathbf{K}_d\|_F$. The requested stiffness is reproduced exactly when $\mathrm{vec}(\mathbf{K}_{x,\mathrm{des}})$ lies in the range of $\mathbf{M}$, that is when $\mathbf{M}\mathbf{M}^*\,\mathrm{vec}(\mathbf{K}_{x,\mathrm{des}}) = \mathrm{vec}(\mathbf{K}_{x,\mathrm{des}})$, and approximated in the above sense otherwise. When several groups of virtual elements act on a single output point, the stiffness is $\mathbf{K}_x = \sum_g \mathbf{L}_g\mathbf{K}_{d_g}\mathbf{R}_g$, with $\mathbf{L}_g = ((\mathbf{P}\mathbf{J}_x)^*)^T\boldsymbol{\eta}\,\mathbf{J}_{d_g}^T$ and $\mathbf{R}_g = \mathbf{J}_{d_g}(\mathbf{P}\mathbf{J}_x)^*$. Because each unknown is bounded by a different kinematic map, the groups must be inverted jointly rather than separately. Defining $\mathbf{M}_g = \mathbf{R}_g^T \otimes \mathbf{L}_g$, with $\otimes$ the Kronecker product, and stacking horizontally,

$$\begin{bmatrix}\mathrm{vec}(\mathbf{K}_{d_1})\\ \vdots \\ \mathrm{vec}(\mathbf{K}_{d_G})\end{bmatrix} = \begin{bmatrix}\mathbf{M}_1 & \cdots & \mathbf{M}_G\end{bmatrix}^*\mathrm{vec}(\mathbf{K}_{x,\mathrm{des}})\,, \tag{S17}$$

which distributes the requested stiffness optimally across the available groups and can be re-evaluated at each time step to track a time-varying profile.

C.3: Numerical validation

Figure S5 validates the model and the gradient-descent schemes on the three single-finger configurations. Fig. S5**a** shows the element layouts. Fig. S5**b** compares the analytically predicted

stiffness against a finite-difference estimate obtained by perturbing the configuration, as a function of the perturbation magnitude: the second-order expression is the more accurate of the two, and the error of both decreases as the perturbation is refined. Fig. S5**c** reports the Frobenius-norm error of the feed-forward inversion, which remains of the order of 10^{-11}. Fig. S5**d** shows the convergence of the force error under both adaptation schemes, on the stiffness and on the rest configuration, across the three configurations. The same force adaptation schemes on the hand index and thumb are shown in Fig. S6.

C.4: Convergence and admissible step sizes

The adaptation schemes are gradient steps on a loss whose model is exact only instantaneously, since the configuration moves as the parameters change. This section establishes the step sizes for which each scheme is well posed. Throughout, $\mathbf{A}_i = ((\mathbf{P}\mathbf{J}_x)^*)^T \boldsymbol{\eta}\, \mathbf{J}_d^T$ evaluated at iteration i, $\boldsymbol{u}_i = \mathbf{d}_{\text{ref}} - \mathbf{d}_i$, $\boldsymbol{v}_i = \mathbf{A}_i^T \mathbf{n}$, and $e_i = F_i - F_{\text{ref}}$ is the scalar force error along the contact normal. With this notation the contact force of Eq. (S13) reads $\mathbf{f}_{x,i} = \mathbf{A}_i \mathbf{K}_d^{(i)} \mathbf{u}_i$, and the corresponding loss becomes:

$$\mathcal{L} = \tfrac{1}{2} \left\| \mathbf{A}_i \mathbf{K}_d^{(i)} \mathbf{u}_i - \mathbf{f}_{x,\text{ref}} \right\|^2 = \tfrac{1}{2}\, \mathbf{e}_i^T \mathbf{e}_i, \qquad \mathbf{e}_i = \mathbf{f}_{x,i} - \mathbf{f}_{x,\text{ref}}. \tag{S18}$$

Both gradients are obtained by perturbing one parameter at frozen configuration: $\mathbf{d}_i$, and with it $\mathbf{A}_i$, are treated as independent of the parameters, so the terms $\partial \mathbf{d}/\partial \mathbf{K}_d$ and $\partial \mathbf{d}/\partial \mathbf{d}_{\text{ref}}$ are neglected. This instantaneous approximation is the reason the admissible step sizes derived below are necessary conditions on the frozen problem. In both cases the first variation of the loss is $\delta\mathcal{L} = \mathbf{e}_i^T \delta \mathbf{e}_i$, so only $\delta \mathbf{e}_i$ has to be computed.

Stiffness. Perturbing $\mathbf{K}_d^{(i)}$ by $\delta\mathbf{K}$, at fixed $\mathbf{u}_i$, gives $\delta \mathbf{e}_i = \mathbf{A}_i\, \delta\mathbf{K}\, \mathbf{u}_i$ and therefore

$$\delta\mathcal{L} = \mathbf{e}_i^T \mathbf{A}_i\, \delta\mathbf{K}\, \mathbf{u}_i = \left(\mathbf{A}_i^T \mathbf{e}_i\right)^T \delta\mathbf{K}\, \mathbf{u}_i. \tag{S19}$$

This is a scalar of the form $\mathbf{a}^T\,\delta\mathbf{X}\,\mathbf{b}$, whose gradient with respect to $\mathbf{X}$ is $\mathbf{a}\mathbf{b}^T$, so

$$\nabla_{\mathbf{K}_d}\mathcal{L} = \mathbf{A}_i^T\mathbf{e}_i\,\mathbf{u}_i^T, \qquad \mathbf{A}_i^T = \mathbf{J}_d\,\boldsymbol{\eta}^T(\mathbf{P}\mathbf{J}_x)^*. \tag{S20}$$

For a frictionless point contact, $\mathbf{P} = \mathbf{n}\mathbf{n}^T$ and the force is directed along the normal, so $\mathbf{e}_i = e_i\mathbf{n}$ and $\mathbf{A}_i^T\mathbf{e}_i = e_i\mathbf{A}_i^T\mathbf{n} = e_i\mathbf{v}_i$, giving the rank-one form used below. This is an outer product of the sensitivity $\mathbf{v}_i$ and the deflection $\mathbf{u}_i$; since the two need not be aligned, this may leave $\mathbf{K}_d$ asymmetric, addressed in Proposition 5.

Rest configuration. Perturbing $\mathbf{d}_{\text{ref}}$ by $\delta\mathbf{d}_{\text{ref}}$, at fixed $\mathbf{K}_d^{(i)}$, gives $\delta\mathbf{u}_i = \delta\mathbf{d}_{\text{ref}}$ and hence $\delta\mathbf{e}_i = \mathbf{A}_i\mathbf{K}_d^{(i)}\,\delta\mathbf{d}_{\text{ref}} = \mathbf{S}_i\,\delta\mathbf{d}_{\text{ref}}$, where $\mathbf{S}_i := \mathbf{A}_i\mathbf{K}_d^{(i)}$ is the sensitivity of the force to the rest configuration. Therefore:

$$\delta\mathcal{L} = \mathbf{e}_i^T\mathbf{S}_i\,\delta\mathbf{d}_{\text{ref}} = \left(\mathbf{S}_i^T\mathbf{e}_i\right)^T\delta\mathbf{d}_{\text{ref}}. \tag{S21}$$

This is a scalar of the form $\mathbf{c}^T\,\delta\mathbf{y}$, whose gradient with respect to $\mathbf{y}$ is $\mathbf{c}$, so

$$\nabla_{\mathbf{d}_{\text{ref}}}\mathcal{L} = \mathbf{S}_i^T\mathbf{e}_i = \mathbf{K}_d^{(i)T}\mathbf{A}_i^T\mathbf{e}_i. \tag{S22}$$

The two updates therefore read:

$$\mathbf{K}_d^{(i+1)} = \mathbf{K}_d^{(i)} - \alpha\,e_i\,\boldsymbol{v}_i\boldsymbol{u}_i^T, \qquad \mathbf{d}_{\text{ref}}^{(i+1)} = \mathbf{d}_{\text{ref}}^{(i)} - \alpha\,\mathbf{S}_i^T\left(\mathbf{f}_{x,i} - \mathbf{f}_{x,\text{ref}}\right), \tag{S23}$$

with $\mathbf{S}_i = ((\mathbf{P}\mathbf{J}_x)^*)^T\boldsymbol{\eta}\,\mathbf{J}_d^T\mathbf{K}_d^{(i)}$ and $\alpha > 0$ the step size.

Lemma 1 (Preservation of positive definiteness)**.** *Let $\mathbf{K}_d^{(i)}$ be positive definite and set $\lambda_i = \lambda_{\min}\left(\frac{1}{2}(\mathbf{K}_d^{(i)} + \mathbf{K}_d^{(i)T})\right) > 0$ and $\beta_i = |e_i|\,\|\boldsymbol{u}_i\|\,\|\boldsymbol{v}_i\|$.* (a) *If $0 < \alpha < \lambda_i/\beta_i$, then $\mathbf{K}_d^{(i+1)}$ from Eq.* (S23) *is positive definite.* (b) *If in addition $\lambda_i \geq \underline{\lambda} > 0$ and $\beta_i \leq \overline{\beta}$ for $i = 0, \ldots, N-1$, then any constant $0 < \alpha < \underline{\lambda}/\overline{\beta}$ keeps $\mathbf{K}_d^{(i)}$ positive definite for all $i = 0, \ldots, N$.*

Proof. For any unit vector $\boldsymbol{x}$, $\boldsymbol{x}^T\mathbf{K}_d^{(i+1)}\boldsymbol{x} = \boldsymbol{x}^T\mathbf{K}_d^{(i)}\boldsymbol{x} - \alpha e_i(\boldsymbol{x}^T\boldsymbol{v}_i)(\boldsymbol{u}_i^T\boldsymbol{x})$. The first term is at least λ_i, and by Cauchy–Schwarz the second is bounded in magnitude by $\alpha\beta_i$, so $\boldsymbol{x}^T\mathbf{K}_d^{(i+1)}\boldsymbol{x} \geq \lambda_i - \alpha\beta_i > 0$ under the stated condition, proving (a). Under the uniform bounds, $\lambda_i/\beta_i \geq \underline{\lambda}/\overline{\beta}$ for every i, so the condition of (a) holds at each step and (b) follows by induction. □

Proposition 3 (Convergence of stiffness adaptation)**.** *For a frictionless point contact with* $\mathbf{P} = \mathbf{n}\mathbf{n}^T$*, the stiffness update of Eq.* (S23) *produces the error recursion* $e_{i+1} = (1 - \alpha\gamma_i)e_i$ *with* $\gamma_i = \|\boldsymbol{v}_i\|^2\|\boldsymbol{u}_i\|^2$*. The error is therefore convergent if and only if* $0 < \alpha < 2/\gamma_i$*, and monotone if* $0 < \alpha < 1/\gamma_i$*. If* $\gamma_i = 0$ *the error is unchanged.*

Proof. The scalar force along the contact normal follows from Eq. (S13): $F_i = \mathbf{n}^T\mathbf{f}_{x,i} = \mathbf{n}^T\mathbf{A}_i\mathbf{K}_d^{(i)}\boldsymbol{u}_i = \boldsymbol{v}_i^T\mathbf{K}_d^{(i)}\boldsymbol{u}_i$ so the force is a bilinear form in the stiffness, with $\boldsymbol{v}_i$ and $\boldsymbol{u}_i$ fixed by the configuration. Holding the configuration frozen, so that $\boldsymbol{v}_i$ and $\boldsymbol{u}_i$ are unchanged by the update, and substituting the stiffness update of Eq. (S23),

$$F_{i+1} = \boldsymbol{v}_i^T\mathbf{K}_d^{(i+1)}\boldsymbol{u}_i = \boldsymbol{v}_i^T\mathbf{K}_d^{(i)}\boldsymbol{u}_i - \alpha e_i\,\boldsymbol{v}_i^T\big(\boldsymbol{v}_i\boldsymbol{u}_i^T\big)\boldsymbol{u}_i = F_i - \alpha e_i\|\boldsymbol{v}_i\|^2\|\boldsymbol{u}_i\|^2,$$

where the rank-one term collapses because $\boldsymbol{v}_i^T\boldsymbol{v}_i\boldsymbol{u}_i^T\boldsymbol{u}_i = \|\boldsymbol{v}_i\|^2\|\boldsymbol{u}_i\|^2$. Subtracting the constant reference F_{ref} from both sides gives $e_{i+1} = e_i - \alpha\gamma_i e_i = (1 - \alpha\gamma_i)e_i$. The recursion is a scalar contraction, so $e_i \to 0$ if and only if $|1 - \alpha\gamma_i| < 1$, that is $0 < \alpha\gamma_i < 2$; the error additionally keeps its sign at every step when $1 - \alpha\gamma_i > 0$, that is $\alpha\gamma_i < 1$. If $\gamma_i = 0$, either $\boldsymbol{u}_i = \mathbf{0}$, the element is undeflected, or $\boldsymbol{v}_i = \mathbf{0}$, the contact normal lies in the null space of $\mathbf{A}_i^T$: in both cases the update produces no force change. □

Proposition 4 (Convergence of reference adaptation)**.** *For a frictionless point contact with* $\mathbf{P} = \mathbf{n}\mathbf{n}^T$*, the reference update of Eq.* (S23) *produces the error recursion* $e_{i+1} = (1 - \alpha\nu_i)e_i$ *with* $\nu_i = \|\boldsymbol{s}_i\|^2$ *and* $\boldsymbol{s}_i = \mathbf{S}_i^T\mathbf{n}$*. The error is therefore convergent if and only if* $0 < \alpha < 2/\nu_i$*, and monotone if* $0 < \alpha < 1/\nu_i$*. If* $\nu_i = 0$ *the error is unchanged.*

Proof. Eq. (S13) is linear in the rest configuration, $\mathbf{f}_{x,i} = \mathbf{S}_i(\mathbf{d}_{\text{ref}}^{(i)} - \mathbf{d}_i)$, so the scalar force along the contact normal is

$$F_i = \mathbf{n}^T \mathbf{f}_{x,i} = \mathbf{n}^T \mathbf{S}_i \left(\mathbf{d}_{\text{ref}}^{(i)} - \mathbf{d}_i \right) = \boldsymbol{s}_i^T \left(\mathbf{d}_{\text{ref}}^{(i)} - \mathbf{d}_i \right),$$

linear in the rest configuration with $\boldsymbol{s}_i$ fixed by the configuration and the current stiffness. Holding $\mathbf{d}_i$ and $\boldsymbol{s}_i$ frozen and substituting the update $\mathbf{d}_{\text{ref}}^{(i+1)} = \mathbf{d}_{\text{ref}}^{(i)} - \alpha e_i \boldsymbol{s}_i$,

$$F_{i+1} = \boldsymbol{s}_i^T \left(\mathbf{d}_{\text{ref}}^{(i)} - \alpha e_i \boldsymbol{s}_i - \mathbf{d}_i \right) = F_i - \alpha e_i \|\boldsymbol{s}_i\|^2.$$

Subtracting the constant reference F_{ref} from both sides gives $e_{i+1} = (1 - \alpha\nu_i)e_i$. As in Proposition 3 the recursion is a scalar contraction, so $e_i \to 0$ if and only if $|1 - \alpha\nu_i| < 1$, that is $0 < \alpha\nu_i < 2$, and the error keeps its sign at every step when $\alpha\nu_i < 1$. If $\nu_i = 0$ the contact normal lies in the null space of $\mathbf{S}_i^T$ and the update produces no force change. □

Both propositions describe the instantaneous behavior at frozen configuration. In practice $\mathbf{d}$ moves as the parameters change, which is why the step sizes used experimentally are well below the bounds and why several iterations are required.

C.5: Dissipativity under an asymmetric stiffness

A virtual element with symmetric $\mathbf{K}_d$ is passive by construction, since $\mathbf{K}_d$ is then the Hessian of a quadratic potential. The update of Eq. (S23) does not enforce this symmetry, and when $\mathbf{K}_d$ is not symmetric it no longer derives from a potential. The following proposition covers this case directly, showing that the closed loop remains dissipative under sufficient damping regardless.

Proposition 5 (Dissipativity under sufficient damping)**.** *Consider the linearized response about equilibrium,* $\boldsymbol{\xi} := \mathbf{d}_{\text{ref}} - \mathbf{d}$*, under the total damping* $\mathbf{B} \succ 0$ *collecting the physical and the virtual contributions, and reflected inertia* $\mathbf{M} \succ 0$*,*

$$\mathbf{M}\ddot{\boldsymbol{\xi}} + \mathbf{B}\dot{\boldsymbol{\xi}} + \mathbf{K}_d\boldsymbol{\xi} = \mathbf{0}, \qquad \mathbf{K}_d = \mathbf{K}_{\text{sym}} + \mathbf{K}_{\text{skew}},$$

with $\mathbf{K}_{\mathrm{sym}} \succ 0$. *Let* $\mu = \lambda_{\max}(\mathbf{M})$, $\underline{\beta} = \lambda_{\min}(\mathbf{B})$, $\overline{\beta} = \lambda_{\max}(\mathbf{B})$, $\kappa = \lambda_{\min}(\mathbf{K}_{\mathrm{sym}})$, *and let* $\varsigma = \|\mathbf{K}_{\mathrm{skew}}\|_2$ *be the induced 2-norm of the skew part, that is its largest singular value. If*

$$\varsigma \;<\; \underline{\beta}\left(\sqrt{\kappa/\mu} - \overline{\beta}/(2\mu)\right),$$

then the origin is exponentially stable and the element dissipates net energy along every trajectory.

Proof. Let $\varepsilon = \underline{\beta}/(2\mu)$ and take

$$E = \tfrac{1}{2}\dot{\boldsymbol{\xi}}^T\mathbf{M}\dot{\boldsymbol{\xi}} + \tfrac{1}{2}\boldsymbol{\xi}^T\mathbf{K}_{\mathrm{sym}}\boldsymbol{\xi} + \varepsilon\,\boldsymbol{\xi}^T\mathbf{M}\dot{\boldsymbol{\xi}},$$

the mechanical energy of the symmetric part plus a cross term. Differentiating and substituting $\mathbf{M}\ddot{\boldsymbol{\xi}} = -\mathbf{B}\dot{\boldsymbol{\xi}} - \mathbf{K}_d\boldsymbol{\xi}$ in the two terms that carry $\ddot{\boldsymbol{\xi}}$,

$$\dot{E} = \dot{\boldsymbol{\xi}}^T\mathbf{M}\ddot{\boldsymbol{\xi}} + \boldsymbol{\xi}^T\mathbf{K}_{\mathrm{sym}}\dot{\boldsymbol{\xi}} + \varepsilon\dot{\boldsymbol{\xi}}^T\mathbf{M}\dot{\boldsymbol{\xi}} + \varepsilon\,\boldsymbol{\xi}^T\mathbf{M}\ddot{\boldsymbol{\xi}},$$

$$\dot{E} = -\dot{\boldsymbol{\xi}}^T\mathbf{B}\dot{\boldsymbol{\xi}} - \dot{\boldsymbol{\xi}}^T\mathbf{K}_d\boldsymbol{\xi} + \boldsymbol{\xi}^T\mathbf{K}_{\mathrm{sym}}\dot{\boldsymbol{\xi}} + \varepsilon\dot{\boldsymbol{\xi}}^T\mathbf{M}\dot{\boldsymbol{\xi}} - \varepsilon\,\boldsymbol{\xi}^T\mathbf{B}\dot{\boldsymbol{\xi}} - \varepsilon\,\boldsymbol{\xi}^T\mathbf{K}_d\boldsymbol{\xi}.$$

Two simplifications follow from the splitting of $\mathbf{K}_d$. In the last term $\boldsymbol{\xi}^T\mathbf{K}_{\mathrm{skew}}\boldsymbol{\xi} = 0$, because a skew-symmetric form vanishes on its own argument, so it reduces to $-\varepsilon\,\boldsymbol{\xi}^T\mathbf{K}_{\mathrm{sym}}\boldsymbol{\xi}$. In the second and third terms the symmetric parts cancel, since $\dot{\boldsymbol{\xi}}^T\mathbf{K}_{\mathrm{sym}}\boldsymbol{\xi} = \boldsymbol{\xi}^T\mathbf{K}_{\mathrm{sym}}\dot{\boldsymbol{\xi}}$, leaving only the skew contribution. Hence

$$\dot{E} = -\dot{\boldsymbol{\xi}}^T(\mathbf{B} - \varepsilon\mathbf{M})\dot{\boldsymbol{\xi}} - \varepsilon\,\boldsymbol{\xi}^T\mathbf{K}_{\mathrm{sym}}\boldsymbol{\xi} - \dot{\boldsymbol{\xi}}^T\mathbf{K}_{\mathrm{skew}}\boldsymbol{\xi} - \varepsilon\,\boldsymbol{\xi}^T\mathbf{B}\dot{\boldsymbol{\xi}}.$$

Bound the four terms. Since $\varepsilon\mathbf{M} \preceq \varepsilon\mu\mathbf{I} = (\underline{\beta}/2)\mathbf{I}$ and $\mathbf{B} \succeq \underline{\beta}\mathbf{I}$, the first gives $\mathbf{B} - \varepsilon\mathbf{M} \succeq (\underline{\beta}/2)\mathbf{I}$. The second is at least $\varepsilon\kappa\|\boldsymbol{\xi}\|^2$. The two cross terms are bounded by Cauchy–Schwarz by $\varsigma\|\boldsymbol{\xi}\|\|\dot{\boldsymbol{\xi}}\|$, since $\|\mathbf{K}_{\mathrm{skew}}\boldsymbol{\xi}\| \le \varsigma\|\boldsymbol{\xi}\|$, and by $\varepsilon\overline{\beta}\|\boldsymbol{\xi}\|\|\dot{\boldsymbol{\xi}}\|$. Therefore

$$\dot{E} \;\le\; -\tfrac{\underline{\beta}}{2}\|\dot{\boldsymbol{\xi}}\|^2 - \varepsilon\kappa\|\boldsymbol{\xi}\|^2 + (\varsigma + \varepsilon\overline{\beta})\|\boldsymbol{\xi}\|\|\dot{\boldsymbol{\xi}}\|,$$

a quadratic form in $(\|\boldsymbol{\xi}\|, \|\dot{\boldsymbol{\xi}}\|)$. It is negative definite exactly when its discriminant is negative, that is when $(\varsigma + \varepsilon\overline{\beta})^2 < 4 \cdot \frac{\underline{\beta}}{2} \cdot \varepsilon\kappa = 2\underline{\beta}\varepsilon\kappa$. Substituting $\varepsilon = \underline{\beta}/(2\mu)$ turns the right-hand side into $\underline{\beta}^2\kappa/\mu$, and taking square roots gives $\varsigma + \underline{\beta}\,\overline{\beta}/(2\mu) < \underline{\beta}\sqrt{\kappa/\mu}$, which is the stated condition.

The condition also makes E a valid storage function. Writing $\mathbf{z} = [\boldsymbol{\xi}^T, \dot{\boldsymbol{\xi}}^T]^T$ gives $E = \frac{1}{2}\mathbf{z}^T\mathbf{P}\mathbf{z}$ with $\mathbf{P} = \left[\begin{smallmatrix} \mathbf{K}_{\mathrm{sym}} & \varepsilon\mathbf{M} \\ \varepsilon\mathbf{M} & \mathbf{M} \end{smallmatrix}\right]$, and by the Schur complement $\mathbf{P} \succ 0$ if and only if $\mathbf{K}_{\mathrm{sym}} \succ \varepsilon^2\mathbf{M}$, for which $\varepsilon < \sqrt{\kappa/\mu}$ suffices. Since $\varsigma \geq 0$ the stated condition forces $\sqrt{\kappa/\mu} > \overline{\beta}/(2\mu) \geq \underline{\beta}/(2\mu) = \varepsilon$, so $\mathbf{P} \succ 0$. With E positive definite and $\dot{E} \leq -c(\|\boldsymbol{\xi}\|^2 + \|\dot{\boldsymbol{\xi}}\|^2)$ for some $c > 0$, exponential stability and the dissipation inequality follow. $\square$

D: Description of additional experiments

This section contains the description of additional experiments and characterizations supporting the results in the main text, and is divided as follows:

1. **Stiffness sweep with torsional and linear springs**
2. **Softening on contact**
3. **Sigmoidal and polynomial stiffness sweep**
4. **Force prediction for various VMC configurations**

Table S4 and Table S5 collect the element configuration and parameters of every experiment reported in the main text and here.

D.1: Stiffness sweep with torsional and linear springs

Fig. S7 shows the sweeps of the main text on three representative springs values, with loading and unloading shown separately. Fig. S7**a** reports the torsional configuration and Fig. S7**b** the cart-constrained fingertip spring. Both exhibit hysteresis, the unloading branch lying below the loading branch because of static friction between the silicone skin and the load-cell plate.

D.2: Softening on contact

Fig. S8 reports the inverse of the stiffening law of the main text. The finger begins stiff and softens with contact force according to the expression in Eq. (S11). Softening flattens the force-displacement curve as contact develops, the opposite of the stiffening behavior and the regime appropriate to fragile objects.

Table S4: **Virtual element configuration per experiment, single-finger test bed**. One row per figure panel, giving the element configuration, its parameters, and the number of independent repetitions N. Shared protocol: 20 mm descent at 2 mm/s, references at 30°, and virtual damping 0.003 N $\cdot$ m $\cdot$ s/rad.

Panel	Configuration	Parameters	N
Passive compliance			
Fig. 3a	finger-space	$K_\theta = 0.10,\ 0.20,\ 0.60$ N $\cdot$ m/rad; dense sweep of 10 values over $[0.02, 0.60]$	5
Fig. 3b	task-space, cart	$K_c = 10,\ 20,\ 100$ N/m; dense sweep of 10 over $[5, 280]$; cart offset 0.10 m, damping 1.0 N $\cdot$ s/m	5
Fig. 3c	finger-space	$K_\theta = 0.1,\ 0.6$ N $\cdot$ m/rad; start offset $-5, 0, +5$ mm; descent 10 mm	5
Fig. 3d	task-space, cart	$K_c = 100$ N/m fixed; $\phi = 0,\ -30,\ -60°$	5
Online modulation			
Fig. 5a	finger-space	stiffening, $[K_{\min}, K_{\max}] = [0.10, 0.60]$, $\alpha = 0,\ 0.3,\ 2.0$ N^{-1}	5
Fig. 5b	mixed	base $K_\theta = 0.5$ N $\cdot$ m/rad; Gaussian $\sigma = 10$ mm, $A = 0,\ 300,\ 600$ N/m, active over the middle half	5
Sensing and force control			
Fig. 7b	finger-space	transmission identification; stiffness triplets from $K_\theta \in [0.05, 1.0]$ N $\cdot$ m/rad; fingertip forces 0.4 to 1.5 N	200
Fig. 8b	finger-space	$\mathbf{K}_d$-descent, $\alpha = 10^{-4}$; square $0.5 \leftrightarrow 0.8$ N, 30 s holds, 3 cycles	5
Fig. 8c	finger-space	$\mathbf{d}_{\text{ref}}$-descent, $\alpha = 5 \times 10^{-4}$; same reference	5
Fig. 8d	finger-space	open loop, both schemes; staircase $0.4,\ 0.7,\ 1.0$ N, 60 s holds	5
Controller validation			
Fig. 10a	passive, no VMC	printed TPU fingers, soft and hard joints, rest angle 30°	5
Fig. 10b	finger-space	K_θ set once per run from the effective stiffness calibration, piecewise linear interpolation	5
Fig. 10c	finger-space	feed-forward inversion of the local K_n from the TPU curves, offset 0.05 N$\cdot$m/rad; $\boldsymbol{\theta}_{\text{ref}}$-descent for force tracking	5
Supplementary experiments			
Fig. S8	both	extended sweeps, as Fig. 3a and 3b	5
Fig. S9	finger-space	softening, $[0.10, 0.60]$, $\alpha = 0,\ 0.3,\ 2.0$ N^{-1}	5
Fig. S10	task-space	sigmoidal and polynomial laws on the fingertip element, joint elements disabled	5
Fig. S11	task, mixed	40 random trials; $K_t \in [10, 40]$ N/m, $K_\theta \in [0.01, 0.20]$ N $\cdot$ m/rad; 1.5 s averaging	40

Table S5: **Virtual element configuration per experiment, ADAPT Hand**. One row per figure panel, giving the element configuration, its parameters, and the number of independent repetitions N.

Panel	Configuration	Parameters	N
Passive compliance			
Fig. 4a	joint-space	$K_\theta = 0.05,\ 0.20,\ 0.60$ N $\cdot$ m/rad; strum 0.05 m at 0.30 m/s; ramp 3 s	1
Fig. 4b	joint-space	$K_\theta = 0.05,\ 0.30$ N $\cdot$ m/rad; 3×100 g; 5 s log after 3 s settle	1
Online modulation			
Fig. 6a	task-space	uniform 10 N/m $\rightarrow$ radial/ulnar 200 vs 0.1 N/m; thumb at a quarter of the finger stiffness; background $K_\theta = 0.1$; ramp 1 s, record 5 s	1
Fig. 6b	task-space	$K_t = 0.1$ (soft), 150 (stiff), soft$\rightarrow$stiff after closure (adaptive); arm 0.50 m at 0.08 m/s, close at 0.20 m	1
Sensing and force control			
Fig. 7c	task-space	probe $K_{\text{sensing}} = 20$ N/m; sweep 50, 100, 200 N/m; others held at 100 N/m; record 5 s	5
Fig. 9a, b	task-space	close at $K_t = 40$ N/m; $\mathbf{K}_d$-descent $\alpha = 10^{-5}$, $\leq 5\%$ change per tick; targets 0.80, 0.20, 0.02 N; converge below 0.07 N for 1 s; descend 0.15 m	1
Controller validation			
Fig. 10d	joint-space	stiff architecture on all kinematic joints; PC_1 and PC_2 targets	1
Supplementary experiments			
Fig. S7	task, mixed	force-descent convergence, index and thumb, three configurations	—
Fig. S13	task-space	time-resolved force and K_n during the apple grasp	1

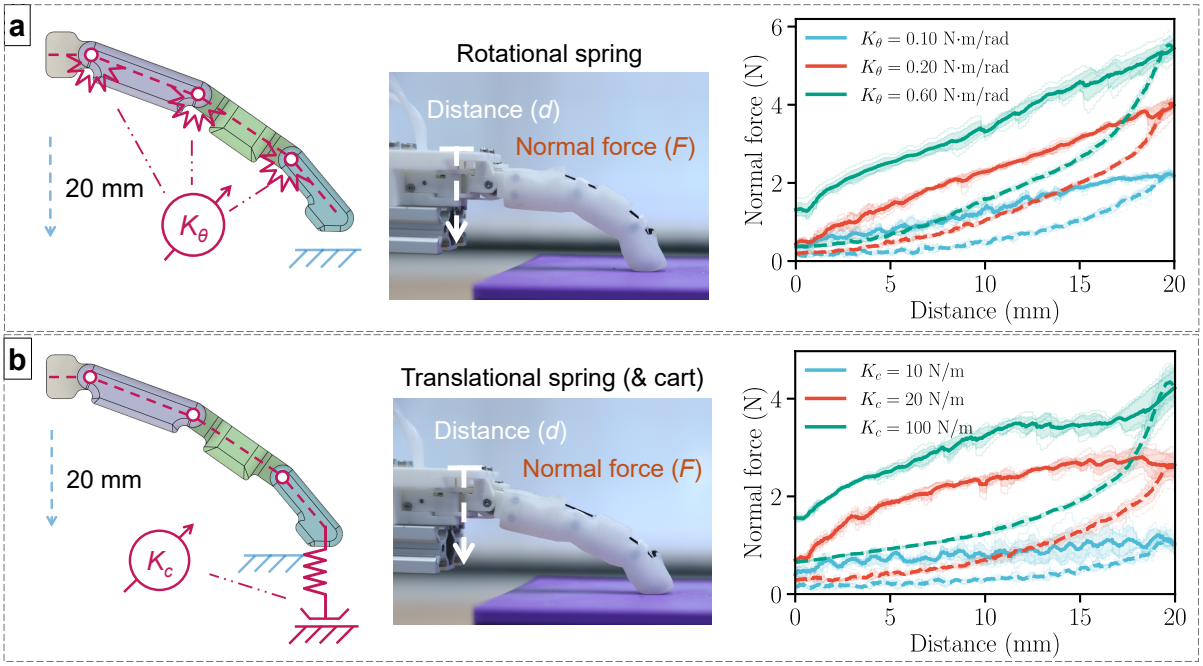

Figure S7: **Extended stiffness sweep on the single-finger platform**. **a** Normal force-displacement profiles for the torsional virtual spring at the finger joints, for $K_\theta = 0.10$, 0.20, and 0.60 N $\cdot$ m/rad. Loading (solid) and unloading (dashed). **b** Normal force-displacement profiles for the translational (cartesian with sliding cart) virtual spring at the fingertip, for $K_c = 10$, 20, and 100 N/m. Loading (solid) and unloading (dashed).

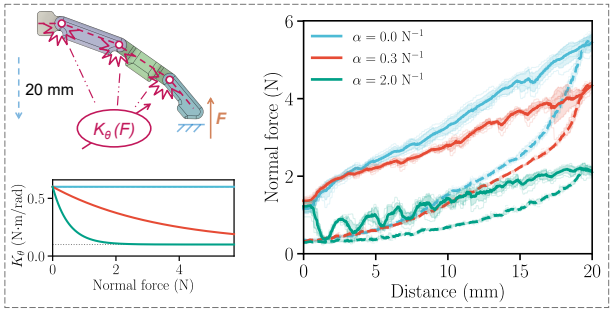

Figure S8: **Softening of the virtual stiffness under contact**. Torsional stiffness at the finger joints decreases with contact force, from $K_{\text{max}} = 0.60$ to $K_{\text{min}} = 0.10$ N $\cdot$ m/rad, for various softening rates, and resulting normal force-displacement curves. Loading (solid) and unloading (dashed).

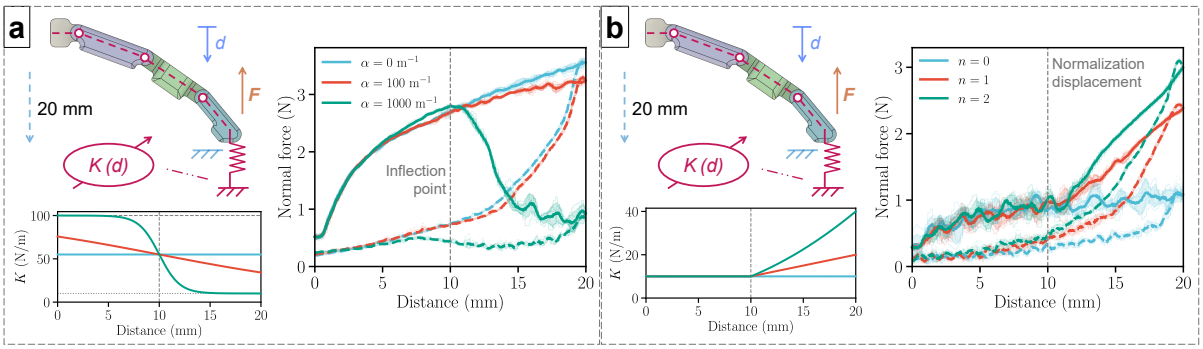

Figure S9: **Displacement-dependent stiffness laws: sigmoidal switch and polynomial increase**. **a** Sigmoidal stiffness law transitioning between a maximum and a minimum stiffness around an inflection point, for different steepness. **b** Polynomial stiffness law of increasing order in displacement, and resulting normal force-displacement curves, normalized to the reference displacement.

D.3: Sigmoidal and polynomial stiffness sweep

Stiffness may also be scheduled on displacement rather than on force, which requires no force measurement at all and, by Eq. (S7), preserves passivity. Fig. S9 reports two such laws applied to a single task-space element at the fingertip. The sigmoidal law of Eq. (S9) switches between two regimes around a threshold displacement, the rate α setting the sharpness of the transition (Fig. S9**a**). The polynomial law of Eq. (S8) grows as a power of normalized displacement, clamped below at K_{min} when d is lower than 10 mm. The order p sets how superlinear the response becomes (Fig. S9**b**). Both shape the force-displacement curve into forms unattainable with a fixed linear element, using the same hardware and only a change of software.

D.4: Force prediction for various VMC configurations

The transmission efficiency was identified on the finger-space configuration. We tested whether it transfers to the others. Fig. S10 shows the task-space (Fig. S10**a**) and mixed-space layouts (Fig. S10**b**). In each, forty trials were run with stiffness drawn uniformly from $[10, 40]$ N/m in task space and $[0.01, 0.20]$ N $\cdot$ m/rad in joint space, each trial averaged over a 1.5 s window

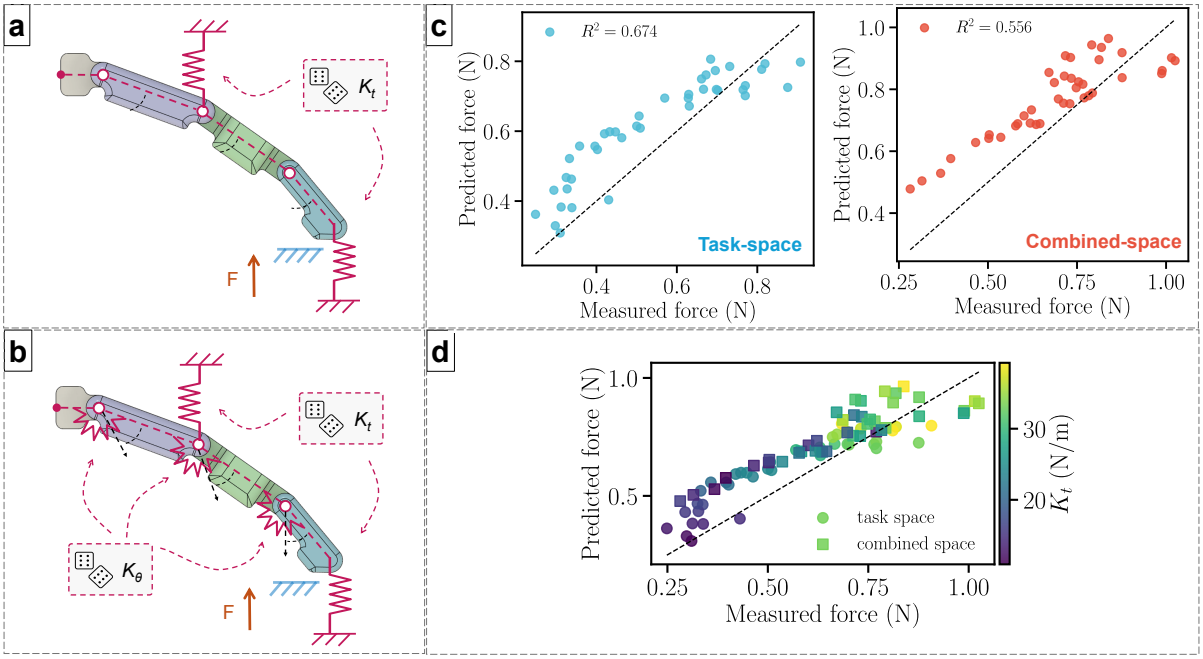

Figure S10: **Force prediction accuracy for task-space and combined-space VMC configurations.**. **a** Task-space virtual element configuration, with cartesian spring at the finger joints. **b** Combined-space configuration, superimposing task-space and joint-space virtual elements. **c** Predicted versus measured normal force for the task-space (left) and combined-space (right) configurations, across randomized stiffness trials. **d** Combined scatter of predicted versus measured force for both configurations, colored by the task-space stiffness K_t.

after settling. Fig. S10**c** compares predicted against measured normal force, while Fig. S10**d** combines the two scatter plots of both configurations, colored by the task-space stiffness K_t. Although with a lower accuracy compared to the baseline, the prediction maintains an accuracy above 67% and 55% in the two respective cases, as $\boldsymbol{\eta}$ characterizes the transmission rather than the particular choice of virtual elements. This licenses its use in the hand experiments, where the elements are cartesian rather than torsional.

E: Description of videos

Supplementary Movie 1: Programmable passive compliance with torsional virtual elements. Single-finger test bed under torsional virtual springs at MCP, PIP, DIP. The arm presses the finger onto the load cell and returns while the shared stiffness K_θ is varied between trials.

Supplementary Movie 2: Programmable passive compliance with cartesian virtual elements. Single-finger test bed under a cartesian virtual spring at the fingertip, constrained to a virtual cart. The arm presses the finger onto the load cell and returns while the stiffness K_c is varied between trials.

Supplementary Movie 3: Guitar strumming across stiffness regimes (with sound). The ADAPT Hand holds a fixed posture under torsional virtual springs while the arm performs a single upward strum. The posture before contact is identical in all three trials; only the virtual stiffness differs.

Supplementary Movie 4: Weight bearing under soft and stiff control. The hand holds a hook posture while an operator adds three 100 g loads in succession, first under a compliant and then under a stiff controller.

Supplementary Movie 5: In-hand manipulation by stiffness redistribution. The hand grasps a printed helicoidal cylinder at uniform fingertip stiffness, then redistributes stiffness towards the radial and subsequently the ulnar digits. The object reorients with no change of grasp pose.

Supplementary Movie 6: Dynamic grasping under three stiffness schedules. The arm translates continuously at 8 cm$/$s while the hand closes onto a yarn ball without interrupting the

motion, under a stiff, a soft, and an adaptive schedule.

Supplementary Movie 7: Sensorless estimation of object compliance. The hand grasps a rigid printed sphere, a kitchen sponge, and a yarn ball, probing each at low thumb stiffness and then squeezing at increasing thumb stiffness while the opposing digits hold.

Supplementary Movie 8: Grip-force regulation while picking an apple. The hand closes on an apple suspended from an elastic band and adapts its fingertip stiffness by gradient descent towards a firm, medium, or light force target, before the arm descends and loads the band.

Supplementary Movie 9: Replication of passive elastic fingers. Force-displacement characterization of the two printed TPU fingers used as physical references, for both the soft and hard passive mechanisms.

Supplementary Movie 10: Pose tracking in free space. With no contact, the same virtual elements act as a distributed position controller. Two targets are tracked, taken from the first two principal components of human grasp postures, with no mode switch separating this regime from other ones.

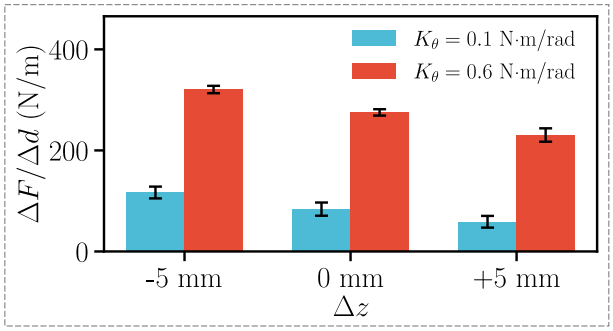

Figure S11: **Effective stiffness of the torsional virtual spring across initial finger poses**. Effective stiffness for the shifted initial poses ($\Delta z = -5$, 0, $+5$ mm) of Fig. 3**c**, for $K_\theta = 0.1$ and 0.6 N $\cdot$ m/rad.

F: Description of further results

This section reports additional results related to the experiments of the main text:

1. **Effective stiffness during pose sweep**

2. **Force and stiffness evolution during grasp adaptation**

F.1: Effective stiffness during pose sweep

Fig. S11 reports the effective stiffness $\Delta F/\Delta d$, obtained by linear regression of force against imposed arm displacement over the descent window, for the three initial arm heights and both virtual stiffnesses. The effective stiffness increases as the finger begins closer to the plate, since the torsional elements are already more deflected at the onset of contact, and the separation between the two K_θ conditions is preserved across poses. Modulation authority is therefore retained across the workspace even though absolute values shift with configuration, a direct consequence of the configuration dependence of $\mathbf{J}_x$ in Theorem 1.

F.2: Force and stiffness evolution during grasp adaptation

Fig. S12 resolves in time what the main text reports only at its endpoints for the apple grasp experiment. Fig. S12**a** shows the mean estimated fingertip force during gradient-descent adapta-

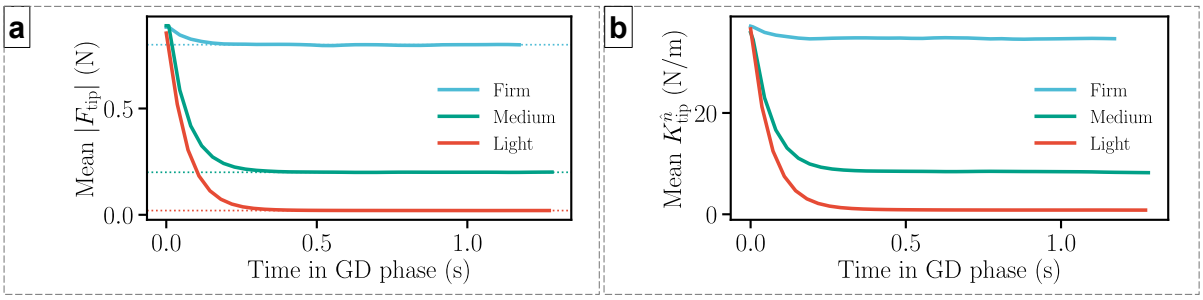

Figure S12: **Time evolution of the estimated fingertip force and stiffness during gradient-descent adaptation of the apple grasp**. **a** Mean magnitude of the estimated fingertip force during the gradient-descent adaptation phase, for the firm, medium, and light grasp targets (cf. Fig. 9). **b** Mean estimated fingertip stiffness, projected onto the normal direction, during the same adaptation phase for the three grasp conditions.

tion for the firm, medium, and light targets. Fig. S12**b** shows the corresponding mean estimated fingertip stiffness, projected onto the contact normal as $K_n = \mathbf{n}^T \mathbf{K}_x \mathbf{n}$. All three conditions converge monotonically and without overshoot, the light target requiring the largest excursion in stiffness. The stiffness trajectories make explicit what the force targets imply mechanically: the three grasps differ not only in the force applied to the apple but in the stiffness with which that force is defended against the elastic disturbance, and it is the latter that determines when the hold is lost during the descent.